POLITECNICO DI TORINO
Repository ISTITUZIONALE

Dual-mode room temperature self-calibrating photodiodes approaching cryogenic radiometer uncertainty

Original
Dual-mode room temperature self-calibrating photodiodes approaching cryogenic radiometer uncertainty / S Ulset, M., Bardalen, E., Pepe, C., Filippo, R., Rajteri, M., Sildoja, M., Kübarsepp, T., Gieseler, J., Gran, J.. - In: METROLOGIA. - ISSN 1681-7575. - STAMPA. - 59:3(2022), p. 035008. [10.1088/1681-7575/ac6a94]

Availability:
This version is available at: 11583/2971654 since: 2022-09-23T09:00:05Z

Publisher:
IOP Publishing

Published
DOI:10.1088/1681-7575/ac6a94

Terms of use:

This article is made available under terms and conditions as specified in the corresponding bibliographic description in the repository

Publisher copyright

(Article begins on next page)

16 October 2026

Metrologia

PAPER • OPEN ACCESS

Dual-mode room temperature self-calibrating photodiodes approaching cryogenic radiometer uncertainty

To cite this article: Marit S Ulset *et al* 2022 *Metrologia* **59** 035008

View the article online for updates and enhancements.

You may also like

- Enhancing the thermoelectric performance through the mutual interaction between conjugated polyelectrolytes and single-walled carbon nanotubes
Shuxun Wan, , Zhongming Chen et al.

- Highly flexible and excellent performance continuous carbon nanotube fibrous thermoelectric modules for diversified applications
Xiao-Gang Xia, , Qiang Zhang et al.

- Intercomparison between the NIST LBIR Absolute Cryogenic Radiometer and an Optical Trap Detector
S R Lorentz and R U Datla

This content was downloaded from IP address 193.204.114.64 on 23/09/2022 at 09:53

OPEN ACCESS
IOP Publishing | Bureau International des Poids et Mesures Metrologia

Metrologia **59** (2022) 035008 (15pp) https://doi.org/10.1088/1681-7575/ac6a94

Dual-mode room temperature self-calibrating photodiodes approaching cryogenic radiometer uncertainty

Marit S Ulset[1,*], Eivind Bardalen[2], Carlo Pepe[3,4], Roberto Filippo[3], Mauro Rajteri[3], Meelis-Mait Sildoja[5,6], Toomas Kübarsepp[5], Julian Gieseler[7] and Jarle Gran[1]

[1] Justervesenet, Fetveien 99, 2007 Kjeller, Norway
[2] University of South-Eastern Norway, Borre, Norway
[3] Istituto Nazionale di Ricerca Metrologica, Torino, Italy
[4] Politecnico di Torino, Torino, Italy
[5] Metrosert, Tallinn, Estonia
[6] National Institute of Chemical Physics and Biophysics, Tallinn, Estonia
[7] Physikalisch-Technische Bundesanstalt, Berlin, Germany

E-mail: mas@justervesenet.no

Received 14 December 2021, revised 24 March 2022
Accepted for publication 26 April 2022
Published 20 May 2022

Abstract

The room temperature dual-mode self-calibrating detector combines low-loss photodiodes with electrical substitution radiometry for determination of optical power. By using thermal detection as a built-in reference in the detector, the internal losses of the photodiode can be determined directly, without the need of an external reference. Computer simulations were used to develop a thermal design that minimises the electro-optical non-equivalence in electrical substitution. Based on this thermal design, we produced detector modules that we mounted in a trap structure for minimised reflection loss. The thermal simulations predicted a change in response of around 280 parts per million per millimeter when changing the position of the beam along the centre line of the photodiode, and we were able to reproduce this change experimentally. We report on dual-mode internal loss estimation measurements with radiation of 488 nm at power levels of 500 μW, 875 μW and 1250 μW, using two different methods of electrical substitution. In addition, we present three different calculation algorithms for determining the optical power in thermal mode, all three showing consistent results. We present room temperature optical power measurements at an uncertainty level approaching that of the cryogenic radiometer with 400 ppm ($k = 2$), where the type A standard uncertainty in the thermal measurement only contributed with 26 ppm at 1250 μW in a 6 hour long measurement sequence.

Keywords: optical power, photodiodes, self-calibration, radiometry, PQED

(Some figures may appear in colour only in the online journal)

1. Introduction

Silicon photodiodes have for decades been the most common detector used for optical power measurements. Their traceability to the International System of Units (SI), which ensures trust in their measurement response, usually comes

* Author to whom any correspondence should be addressed.

Original content from this work may be used under the terms of the Creative Commons Attribution 4.0 licence. Any further distribution of this work must maintain attribution to the author(s) and the title of the work, journal citation and DOI.

 © 2022 BIPM & IOP Publishing Ltd

from comparison to a cryogenic radiometer (CR), which is a primary standard detector for optical power. The CR is a cooled thermal detector, operating by the principle of electrical substitution. This means that optical power is determined by comparing the temperature rise of the illuminated absorber to the electrical power needed to produce an equivalent rise in temperature. The CR is a reliable and well-established primary standard, with measurement uncertainties in the order of 200 parts per million (ppm) [1]. However, CRs are bulky, operated at low temperatures and require high expertise for operation.

Photodiodes on the other hand are small, quick and easy to operate, and are typically used directly on the application level. For an ideal, lossless photodiode, each absorbed photon will produce one electron in the measurement circuit. However, real photodiodes have losses that must be accounted for when calculating the responsivity of the photodiode. This is typically done by calibration against an external reference, which means that photodiodes depend on primary standards such as the CR for traceability. However, if one could determine the losses of the photodiode using only the physics of the photodiode itself, there would be no need for an external reference, and the detector would be self-calibrated.

The history of self-calibrating photodiodes started around 1979, when Geist [2] proposed a method for determining the internal losses of a photodiode from purely relative measurements at different wavelengths, and combining these with an analytical expression for the internal losses. Another method, based on applying a voltage bias to the photodiode and oxide surface, followed shortly by Zalewski and Geist in 1980 [3].

Around the same time as this early work on self-calibration of photodiodes, Hansen [4] presented the induced-junction photodiode. This is the type of photodiode used in this paper. Instead of having a doped layer close to the surface, the induced-junction photodiode consists only of a lightly p-doped silicon substrate with a thermally grown oxide layer on top. Positive charges in the oxide induce an n-type layer below the interface and a pn-junction is formed.

The next step in the self-calibration of photodiodes, when the internal losses were being reduced, was to find a way to determine the losses that still remained. Geist and co-workers worked with modelling of the internal losses in the early years of self-calibration [2, 5], and from the 1990s computer software was used to model the losses with increasing accuracy [6–9]. Methods exploiting spectrally invariant detectors and fitting with an analytical model demonstrated an estimated uncertainty limited by the properties of the photodiode to around 0.02% [10].

Geist *et al* [6] presented in 2003 a thorough review of each of the terms contributing to the quantum deficiency of photodiodes. This work was essential for the initiation of the QuCandela project [11] from 2008–2011, where the predictable quantum efficient detector (PQED) [12, 13] was developed, as a high-accuracy optical power trap detector based on induced-junction photodiodes. The PQED photodiodes are specifically designed to have low and predictable losses, where internal losses are predicted using numerical tools such as 1D computer simulations [14]. The *mise en pratique* for the definition of the candela [15] has now adopted the PQED as a primary standard.

A new step in the self-calibration development was made when White *et al* [16] proposed the novel idea of combining the measurement principle of the PQED with that of a CR, in one dual-mode detector. They stated uncertainties in the percentage level at cryogenic temperature. This method was improved by one order of magnitude at room temperature by Nordsveen *et al* [17].

The dual-mode detector can, by combining a photodiode with a temperature sensor, a weak heat link and a heat sink, measure incident radiation either thermally or photoelectrically. Since the same absorber is used in both modes, the dual-mode detector enables a comparison measurement between two primary methods with an accuracy not achievable with two different detectors. The uncertainty is further reduced by using the same measurement electronics in both modes of operation. Furthermore, the combination of the two methods in one detector opens up new advantages and possibilities. The dual-mode detector can be used to measure broadband sources as well as monochromatic sources, as it gives a direct measurement of the source-specific response in ampere per watt (A W^{-1}).

As a follow-up to the development of the PQED the chipS·CALe project was launched in 2019 [18], with the aim of exploiting both thermal and photo-electrical measurement methods in one device. The project has successfully manufactured improved low-loss induced-junction photodiodes [19] and has improved and demonstrated a robust 3D charge-carrier simulation method for prediction of the internal losses with unprecedented uncertainties at the 20 ppm level [20]. The project will also perform a high-accuracy dual-mode measurement at cryogenic temperatures, to link radiometric measurements directly to the SI through the fundamental constants ratio e/h, based on ideas by Brida *et al* [21]. Of more interest to the average users of optical power detectors, the last part of the project aims at developing a fully self-calibrating dual-mode detector, for easy and practical operation in room temperature, with measurement uncertainty below 0.05%, which is the topic of this paper.

We report on the improved thermal design of the room temperature dual-mode detector, with computer simulations of thermal equivalence in electrical substitution. Detectors were assembled according to the new design and measurements at room temperature are presented. We present a new unpublished method for realising the electrical substitution part of the measurement sequence, and we evaluate three different calculation algorithms.

2. The dual-mode self-calibrating measurement

The responsivity $R(\lambda)$ of a real photodiode, in units of A W^{-1}, is given by:

$$R(\lambda) = \frac{e\lambda}{hc} \cdot (1 - \delta(\lambda))(1 - \rho(\lambda))y(\lambda), \tag{1}$$

where e is the elementary charge, λ is the vacuum wavelength of the incoming radiation, h is Planck's constant, and c is the

speed of light. The spectrally dependent loss terms, $\delta(\lambda)$, $\rho(\lambda)$ and $y(\lambda)$, represent the internal loss, reflectance loss and quantum yield, respectively. Quantum yield is mostly of concern for wavelengths below 450 nm [22]. During self-calibration, we are only concerned with the absorbed optical power, which is equal for both modes of the dual-mode detector, and we can disregard the reflectance loss $\rho(\lambda)$. Throughout the manuscript we therefore omit the reflectance term in equation (1) and we also include yield effectively as a part of $(1 - \delta(\lambda))$. It is important to note that for absolute power measurements the reflectance loss must be taken into account.

In this work, the focus is on the internal loss, $\delta(\lambda)$, also referred to as the internal quantum deficiency (IQD). $\delta(\lambda)$ is determined through the self-calibration procedure of the dual-mode detector, where thermal mode is used as a reference.

2.1. Mode 1: photocurrent mode

In photocurrent mode the optical power, P_{PC}, is found from the measured photocurrent i_{photo} and the responsivity $R(\lambda)$:

$$P_{\mathrm{PC}} = \frac{i_{\mathrm{photo}}}{R(\lambda)}. \tag{2}$$

This means that the absorbed optical power is instantly known from a photocurrent measurement when the spectral response of the detector and spectral distribution of the radiation is known.

2.2. Mode 2: thermal mode

In the thermal mode of the dual-mode detector, we use the principle of electrical substitution, where the optical power is determined by replacing optical heating with an equivalent amount of electrical heating. In conventional electrical substitution radiometers, electrical heating is done with an external heater. However, since our absorber element is a photodiode, we use the photodiode itself as a heater by exploiting its resistive properties. By applying a forward bias (FB) voltage, a current will flow and produce Joule heating. In this way, the heat is deposited inside the photodiode structure. Using the photodiode as the heater allows us to use the same circuitry and instrumentation both to measure the photocurrent and the forward heating current, reducing the uncertainty contribution from the instruments.

The absorbed optical power in thermal mode, P_{opt}, is estimated from the equivalent thermal response with electrical power, $P_{\mathrm{el}} = VI$, where V is the measured voltage across the photodiode and I is the measured current through the photodiode.

By using two different levels of electrical power, one slightly above and one slightly below the optical power level, the optical power can then be found from a linear fit based on the two electrical levels in the following way:

$$P_{\mathrm{opt}} = \frac{(T_{\mathrm{opt}} - T_1)}{(T_2 - T_1)}(P_2 - P_1) + P_1. \tag{3}$$

Here, T_{opt} is the temperature signal during optical heating, and T_1, T_2, P_1 and P_2 are the temperature signals and electrical powers of the low and high electrical heating levels, respectively.

2.3. Determining internal losses of the photodiode

The IQD of the photodiode, $\delta(\lambda)$, is determined by combining equations (1) and (2), giving the following expression:

$$\delta(\lambda) = 1 - \frac{i_{\mathrm{photo}}}{P_{\mathrm{opt}}} \cdot \frac{hc}{e\lambda}. \tag{4}$$

Here the dual-mode self-calibration comes into action, as we use thermal mode as a reference, replacing the absorbed power in photocurrent mode P_{PC} with the absorbed power from thermal mode, P_{opt} from equation (3). As can be seen from equation (4), the IQD depends on wavelength, photocurrent and power level. However, in the linear range of the detector, where i_{photo} is proportional to P_{opt}, the IQD depends solely on wavelength. This means that only one thermal measurement is required to determine the IQD for the linear range for one specific wavelength. Furthermore, outside the linear range, one measurement point will determine the IQD at that specific power level. If an extended dynamic range is needed, this can be achieved by including more measurement points.

3. Detector design and assembly

In electrical substitution, the thermal response must be equal for both electrical and optical heating. In the dual-mode detector, optical heating happens in the centre of the photodiode while electrical heating is deposited around the edges of the photodiode. This gives different heating profiles and causes a non-equivalence in the thermal response. To account for this we have used computer simulations to develop an optimised thermal design that ensures minimum thermal non-equivalence and equal response for electrical and optical heating.

3.1. Detector module

The dual-mode detector design was developed with the aid of thermal simulations using COMSOL Multiphysics. The assembly is shown schematically in figure 1(a). The chipS·CALe p-type induced-junction photodiode with a SiN_x oxide layer with an active area of 11 mm × 14 mm was used [19]. Preliminary tests of these photodiodes show that they have a record low IQD in the sub 20 ppm range and linearity up to several milliwatts when sufficiently biased. The outer physical dimensions of the photodiode are 13.1 mm × 16.1 mm × 500 μm.

The photodiode is thermally connected to the heat sink with a polyimide printed circuit board (PCB), via a silicon thermal diffuser structure. The layout of the PCB is shown in figure 1(b). The PCB contains seven electrical pads for wire connections to external instruments. Five traces are used for electrical biasing and current readout from the photodiode. The current traces each have a width of 100 μm, while each voltage trace has a width of 60 μm and connects to the current traces

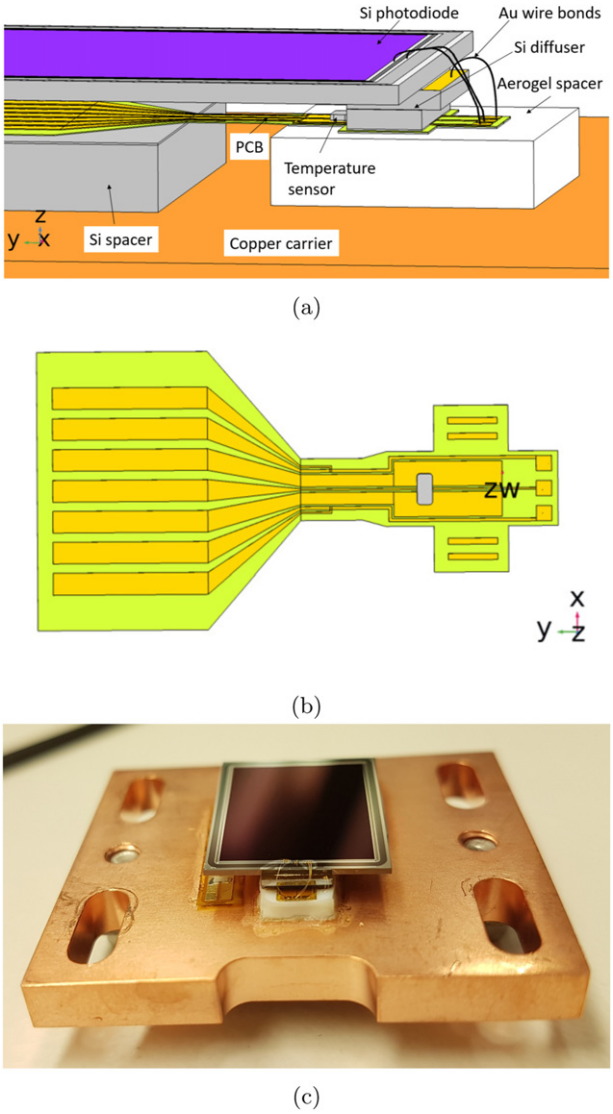

Figure 1. (a) CAD model of the DMD structure. (b) CAD model of the PCB layout, also showing the position of the soldered temperature sensor. (c) Image of the assembled dual-mode detector module.

such that the electrical measurements and control are done in a four-probe setup. Additionally, one pad connects to the photodiode guard. The two remaining traces have a width of 400 µm each and connect to a Semitec 103FT1005A5P1 thermistor, which is soldered close to the silicon diffuser. The thickness of the PCB traces was measured to 23 µm, of which 20 µm is copper and the top 3 µm is electroless nickel immersion gold (ENIG) coating.

The back side of the PCB is glued on one side to a thermally insulating aerogel spacer which was prepared from Airloy X103 (density class M) material, and on the other side to the heat sink via a silicon spacer, with an air gap between. The dimensions of the electrical traces on the PCB within this gap give a suitable thermal resistance, which partly determines the thermal responsivity of the photodiode (K W^{-1}). The diffuser structure consists of two adhesively bonded pieces of silicon diced from oxidised silicon wafers. The pieces were bonded with Stycast 1266 epoxy using a force of 5 N such that an epoxy layer thickness of around 6 µm was obtained. The top side of the upper silicon piece is coated with a 0.4 µm thick Au layer. The photodiode is bonded with EPO-TEK EJ2189-LV conductive epoxy to this piece such that an electrical connection to the photodiode back side can be made. Au ball-wedge wire bonds with wire diameter 17.5 µm were used to connect the photodiode connection rings and photodiode back side with the PCB.

An image of the assembled dual-mode detector module is shown in figure 1(c).

3.2. Trap structure

To test the properties of the dual-mode detector in a light-trapping form, a wedged structure was designed to hold two detector modules, shown in figure 2, under 45° angle relative to the photodiode active surfaces. In such a configuration the incident beam undergoes three reflections before exiting along the incoming beam. Based on calculations, the fraction of optical power in the back-reflected beam is lower than 0.1% over the spectral range from 425 nm to 725 nm for p-polarized light and even below 0.01% from 460 nm to 570 nm. The low back-reflection ensures that possible inter-reflections will not cause additional error in the setup. The holder has a triangular prism shape with dimensions of 42 mm, 45 mm and 50 mm.

A two-stage approach is used to mount the detector modules to the prism. First, the modules are firmly mounted to a rectangular copper carrier, as shown in figure 1(c), and then the carriers are placed into dedicated recessed areas in the prism shown schematically in figure 2(b). The carriers can be slid uniaxially about ±2.5 mm to achieve proper position for the photodiodes. At the suitable position the carriers are fixed using four screws. The prism is then mounted either to a vacuum chamber or to a cryostat. The angles between the planes of recesses in the prism were measured using a 3D coordinate measuring machine. Results showed that the angles are in the range from 44.9° to 45.0°, which is sufficiently accurate for our needs.

4. Detector modelling

4.1. Heat transfer simulations

The thermal response of the module was simulated using COMSOL Multiphysics. Optical heating was simulated using a heat source with power P_{opt} in the active area of the photodiode. The optical beam was modelled as a heat source with uniform power density in a thin volume on the surface of the photodiode, having an elliptical outline corresponding to the 45° incident angle. The electrical heating was simulated as a heat source with power P_{el} between the contact rings around the edges of the photodiode. In addition, the effect of parasitic heating of the PCB traces and wire bonds was simulated by applying a current i given by the power–current relation of the photodiode in FB.

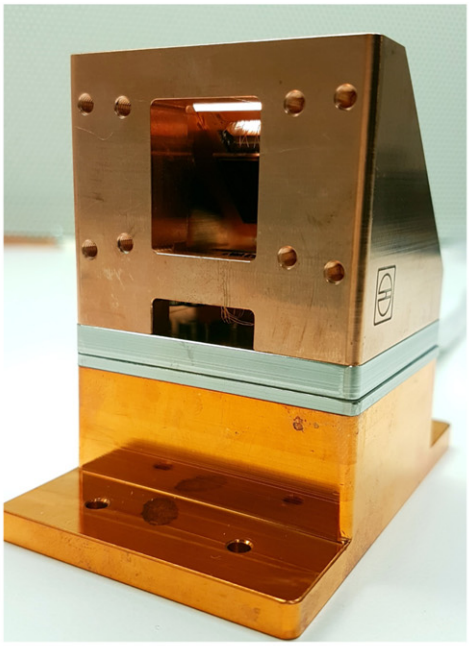

(a)

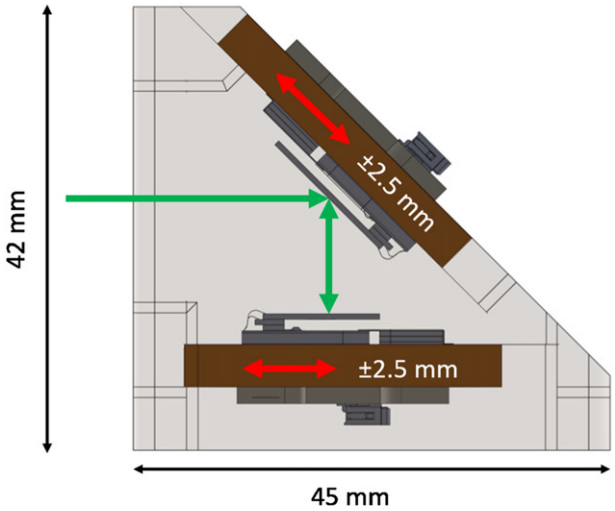

(b)

Figure 2. (a) Image of the copper trap structure. (b) Side-view schematic showing dimensions of the trap structure. Green arrows show laser beam path, while red arrows indicate direction of possible adjustment of the two detector modules.

Radiative cooling, j, of the photodiode surface was modelled according to

$$j = \sigma\varepsilon(T^4 - T_0^4) \tag{5}$$

where σ is the Stefan–Boltzmann constant, ε is the emissivity of the photodiode, T is the temperature of the photodiode surface and T_0 is the ambient temperature. On the parts of the photodiode covered by aluminium, including the back side of the photodiode and photodiode contact rings, an emissivity value of 0.05 was used. On the oxidised surfaces and photodiode sidewalls, an emissivity value of 0.42 was used, based on measurements described in section 4.2.

The total net emitted power from thermal radiation, P_{TR}, is found by integrating equation (5) over the photodiode surface. The remaining heat flow, P_{cond}, is dissipated to the heat sink with solid conduction:

$$P_{\mathrm{cond}} = P_{\mathrm{tot}} - P_{\mathrm{TR}}. \tag{6}$$

Consequently, P_{cond} leads to a temperature rise at the temperature sensor. The thermal responsivity to heating was evaluated as the ratio between the total input power P_{tot} and the temperature rise ΔT at the surface of the modelled temperature sensor:

$$R_{\mathrm{th}} = \Delta T / P_{\mathrm{tot}}. \tag{7}$$

In optical heating, $P_{\mathrm{tot}} = P_{\mathrm{opt}}$, while in electrical heating $P_{\mathrm{tot}} = P_{\mathrm{el}} + v \cdot i$, where $v \cdot i$ represents the Joule heating of the PCB traces and wire bonds between the voltage sensing point and the photodiode contacts.

The thermal non-equivalence γ can then be defined as the relative difference in responsivity between optical and electrical heating:

$$\gamma = \frac{R_{\mathrm{th,opt}} - R_{\mathrm{th,el}}}{R_{\mathrm{th,el}}}. \tag{8}$$

For a given optical power level, γ is found by setting $P_{\mathrm{el}} = P_{\mathrm{opt}}$. Typically, the change in $R_{\mathrm{th,el}}$ caused by the additional heating term $v \cdot i$ in electrical heating mode is less than 1 ppm, and is therefore negligible.

Figures 3(a) and (b) show the simulated non-equivalence in the detector assembly for a centred uniform beam with a beam diameter of 1.5 mm, with absorbed power $P_{\mathrm{opt}} = 1$ mW. While the maximum non-equivalence in the photodiode itself exceeds 10 000 ppm, it is reduced to around 300 ppm at the position of the temperature sensor. The reason for this is the diffuser structure, which significantly reduces the non-equivalence in heat flow. This is evident from figure 4, which shows a streamline plot of the conductive heat flow.

Figure 5(a) shows the thermal non-equivalence as a function of beam position on the photodiode, where $y = 0$ corresponds to the centre of the photodiode. The dependence on beam position follows from the difference in the temperature profile on the photodiode surface between the optical and electrical heating modes, as illustrated in figure 5(b). The optical heating leads to a hot spot in the centre, while in the electrical heating mode, the temperature across the photodiode surface is more uniform. As a consequence, there is a difference in emitted thermal radiation between the two heating modes. This difference in radiation is the main source of non-equivalence during electrical substitution.

The high dependence on beam alignment in the y-direction seen in figure 5(a) is caused by the asymmetry from the silicon diffuser being located on one edge of the module. The high degree of symmetry of the assembly in the x-direction gives a low sensitivity to beam alignment in this direction. The non-equivalence in thermal radiation loss, and hence in P_{cond}, explains the dependence on displacement of the simulated non-equivalence of around 280 ppm mm^{-1} seen in figure 5(a). The sensitivity of the non-equivalence to beam size is minor, only changing the offset in figure 5(a) by about 30 ppm when

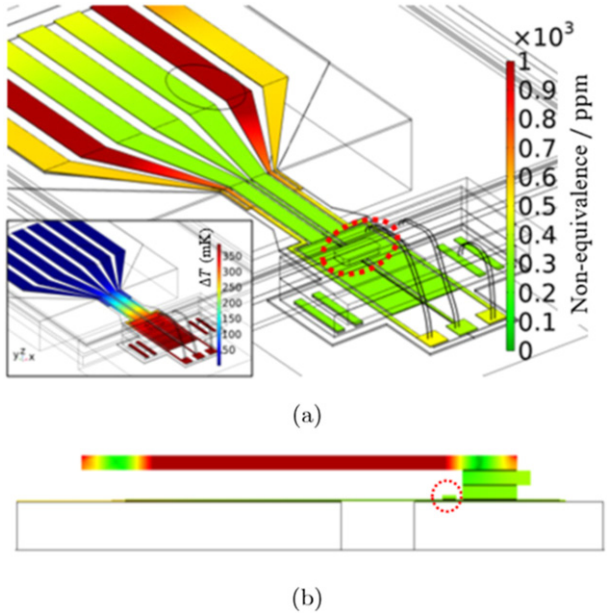

Figure 3. Simulated non-equivalence in ppm (absolute values) as seen in the (a) PCB traces and temperature sensor and (b) in the cross-section of the dual-mode detector. Colour scale has been limited to maximum 1000 ppm and is common for (a) and (b). The red circles in (a) and (b) indicate the position of the temperature sensor. Inset in (a) shows the temperature ΔT in the PCB traces.

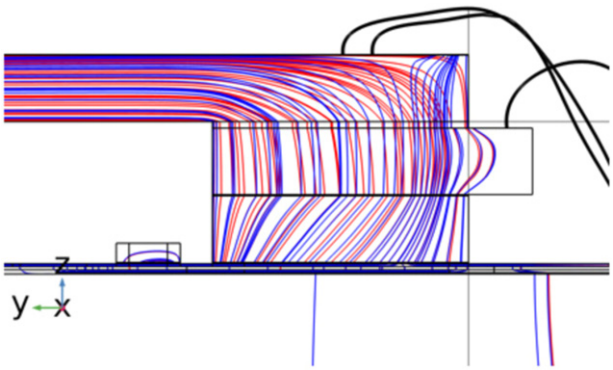

Figure 4. Streamline plot of the conductive heat flow near the diffuser structure. Red and blue lines show thermal conduction in optical and electrical heating modes respectively.

increasing the beam diameter from 0.5 mm to 3 mm. Furthermore, there is a shift of less than 10 ppm when changing between a Gaussian and cylindrical power distribution.

A small part of the contribution to non-equivalence, around 35 ppm, is due to resistive heating of wires in electrical heating mode. Simulations show that the wire bonds contribute to around 400 ppm of the measured electrical heating, while the PCB traces contribute to around 200 ppm. However, the thermal design and placement of the voltage traces ensure that this heat is largely accounted for in the temperature measurement.

Figure 6 shows a plot of the thermal non-equivalence and the thermal responsivity of the dual-mode detector as a function of input power. The non-equivalence changes by less than 40 ppm from input powers between 0.5 mW and 20 mW. In the same range, the thermal responsivity decreases by less than 1%.

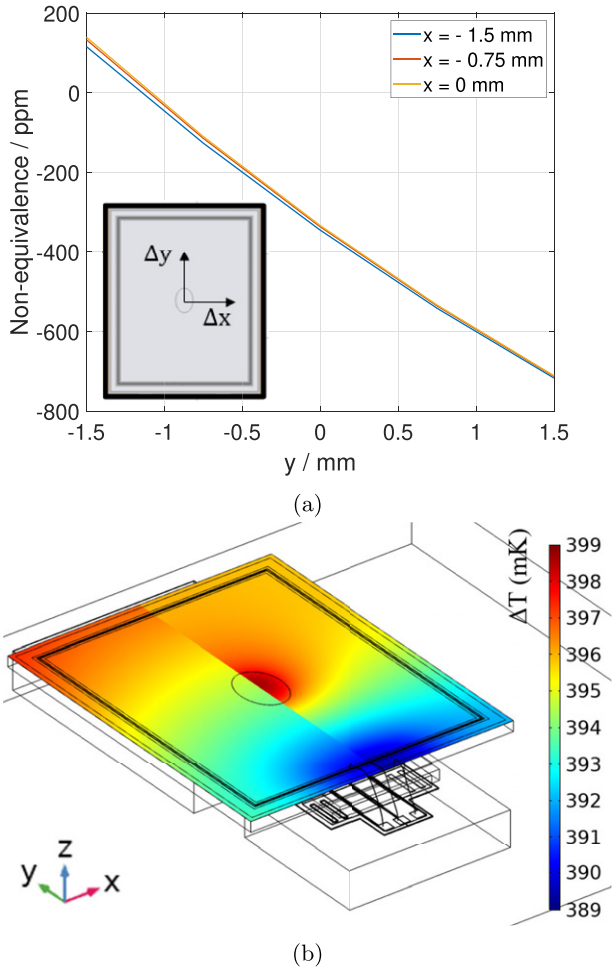

Figure 5. (a) Non-equivalence as a function of beam position on the photodiode. Inset shows the directions of the displacement x and y on the photodiode. (b) Simulated photodiode surface temperature increase ΔT in mK for 1 mW absorbed power. Left side shows the result for electrical heating, while right side shows the result for optical heating.

The simulated time constant of the module at 290 K is 86 s. By changing the dimensions of the PCB traces, the time constant, and thereby thermal responsivity, can be tuned. The time constant is temperature dependent and reduces to 4 s at 40 K in a non-linear way based on material properties. At 40 K, due to the high increase in thermal diffusivity and insignificant thermal emission, the predicted non-equivalence is below 1 ppm and is insensitive to beam alignment.

4.2. Emissivity measurement

To calculate the radiative heat loss, knowledge of the total hemispherical emissivity ε of the photodiode is required. For this, a sample wafer was characterised at the Emissivity Measurement under Air Facility at Physikalisch-Technische Bundesanstalt (PTB) in Berlin. The setup and evaluation scheme are described in detail in references [23, 24].

The sample was kept constant at 20.5 °C. Spectral directional emissivity was measured from 5 µm to 25 µm with a Fourier-transform infrared (FTIR) spectrometer of the Michelson type equipped with a pyroelectric DLaTGs detector and

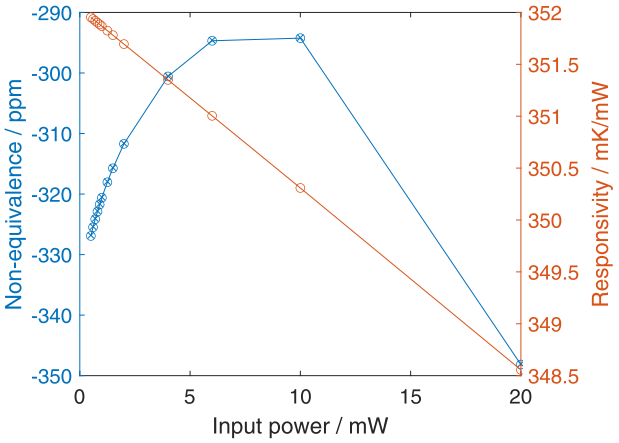

Figure 6. Thermal non-equivalence and responsivity dependence on power.

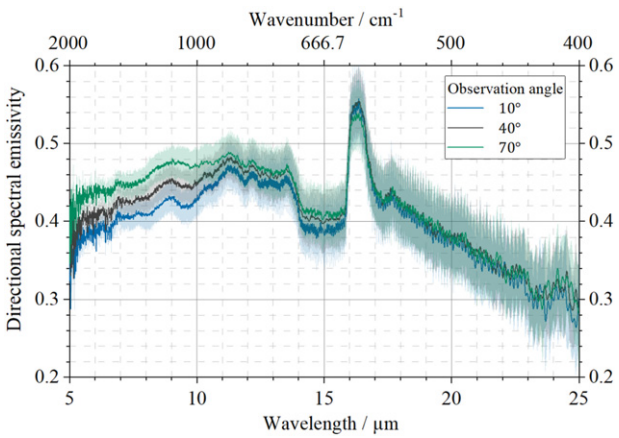

Figure 7. Spectral directional emissivity of the sample wafer at 20.5 °C from 5 µm to 25 µm and under observation angles of 10°, 40° and 70° together with their respective standard uncertainty intervals ($k = 1$).

a KBr beamsplitter and under observation angles relative to the sample surface normal from 10° to 70° in steps of 10°. Figure 7 shows the measured spectral directional emissivity for observation angles of 10°, 40° and 70° with their expanded standard uncertainty intervals. The spectral structure is typical for silicon. A high frequency modulation can be seen, which is especially apparent from 17 µm to 25 µm and is consistent with thin film interference caused by a 500 µm thick layer of silicon. Total hemispherical emissivity was then calculated from spectral directional emissivity to be $\varepsilon = 0.421 \pm 0.033$.

5. Experiment

5.1. Measurement setup

Measurements were performed with a dual-mode detector module as described in section 3.1 and shown in figure 1(c). During measurements the detector module was installed in the upper position in the copper trap structure in figure 2, at a 45° angle with respect to the incoming beam. The trap structure was placed inside a vacuum chamber with a wedged, anti-reflective coated window, and the cube was placed on a stage with adjustable height. Figure 8 shows images of the vacuum cube, the copper trap structure mounted inside the vacuum cube, and the dual-mode detector seen through the window of the cube. The pressure inside the cube was kept at around 10^{-6} mBar using an Agilent Mini-Task AG81 pump.

The optical setup for the dual-mode measurement is shown in figure 9(a). The source used was a krypton ion laser, and the laser beam was stabilised using a laser power controller. The beam size on the detector was roughly 2 mm in diameter ($1/e^2$).

The position of the beam on the detector surface was changed by moving the vacuum cube up and down on an adjustable stage while monitoring the height with a dial indicator. The midpoint of the photodiode was found by edge detection using the drop in the photocurrent.

Figure 9(b) shows the electrical scheme of the setup and instruments used. The copper trap structure was temperature controlled using a Thorlabs TED 350 temperature controller together with a peltier element, to a temperature slightly below room temperature. The input for the controller was the signal from a thermistor on the copper carrier (figure 1(c)). The voltage source used for both reverse biasing in photocurrent mode and forward biasing during electrical heating was a Datron 4700 calibrator. The current was converted to voltage with a Femto DLPCA-200 transimpedance amplifier and the voltages were measured with a Keithley 2002 digital multimeter using a scanner card. Temperature was measured using a SIM921 AC resistance bridge from Stanford Research Systems. All wiring between the vacuum cube and instruments were shielded twisted pairs, and all electrical circuits and shields were carefully grounded to reduce noise.

5.2. Measurement procedure

Measurements were performed with radiation of 488 nm wavelength and absorbed optical power of 500 µW, 875 µW and 1250 µW. Photocurrent measurements were performed for every five cycles of thermal measurements. To ensure a saturated photocurrent, a reverse bias of −10 V was applied during all photocurrent measurements.

Electrical substitution was performed by cycling up and down three steps:

(a) Low electrical heating (shutter closed)
(b) Optical heating (shutter open, with or without simultaneous electrical heating)
(c) High electrical heating (shutter closed)

The step height was 5 µW, and the duration of each step was 10 min.

With radiation power of 1250 µW, measurements were performed at different points along the centre of the photodiode by adjusting the height of the detector. The height changes were done in steps of 0.35 mm, corresponding to 0.5 mm steps on the photodiode surface with an incident angle of 45°.

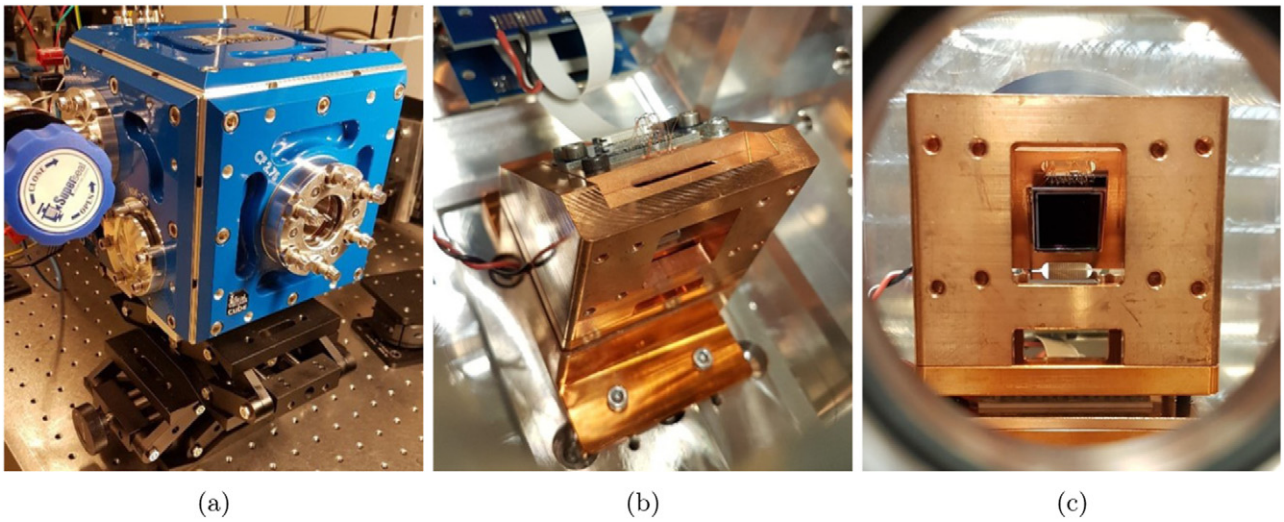

Figure 8. (a) Vacuum cube placed on vertically adjustable stage. (b) Copper trap structure mounted inside the vacuum cube. (c) The dual-mode detector mounted in the upper position of the copper trap structure, seen through the vacuum cube window.

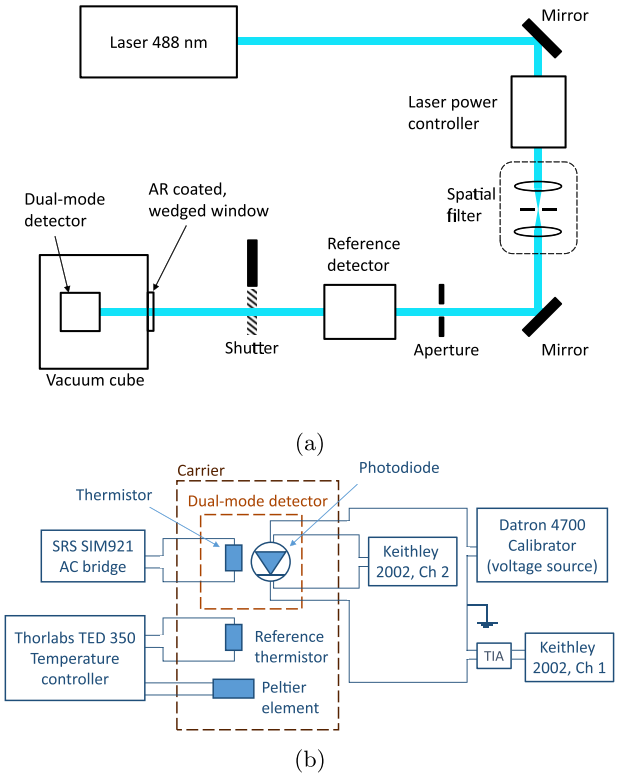

Figure 9. (a) Layout of the optical components in the dual-mode measurement setup. (b) Circuit diagram of electrical connections and instruments.

5.3. Mirror in detector position 2

The original intention was to use two detector modules in the trap configuration to minimise reflection losses. A dual-mode measurement can then be performed on the upper target detector, while we monitor the photocurrent with the second detector. However, optical heating of the monitor detector was found to cause disturbances in the temperature of the target detector. This can be seen in figure 10(a). During optical heating, slightly less than 10% of the incoming optical power is absorbed by the second photodiode. This gives an increase in temperature of the monitor detector module, and this fraction of optical power heats the whole massive copper trap structure, leading to a temperature drift in the target detector module.

One way to remove this disturbance in the thermal distribution is to add an equivalent amount of electrical heating on the monitor detector when the shutter is closed. This will help maintain a steady heat flow from the monitor detector, rather than a heat flow that is switched on and off with the shutter. As shown in figure 10(b), this method improved the signal quality and stability. However, this method of electrically compensating the temperature drift turned out to be tedious and impractical when changing between power levels.

Since the dual-mode measurement on the target detector is not dependent on a signal from the monitor detector, we decided to replace the monitor detector with a mirror. The mirror ensured that most of the optical signal was absorbed in the target detector and we eliminated the drift without having to compensate electrically, as shown in figure 10(c). The increased reflection from replacing the monitor detector with a mirror did not affect the self-calibration measurement as the measurement is purely relative.

5.4. The forward bias and open circuit methods

Step (b) of the electrical substitution (section 5.2) was performed with two different methods, as illustrated in figure 11. In the open circuit (OC) method, which was used in our previous work [17], the electrical circuit is opened during optical heating, so no current can flow. This means all photo-generated charge carriers recombine in the substrate and produce heat.

In the second method, the FB method, we heat the detector electrically during step (b), while simultaneously irradiating the photodiode. The advantage of testing this method is that it can be further developed to include a closed feedback loop

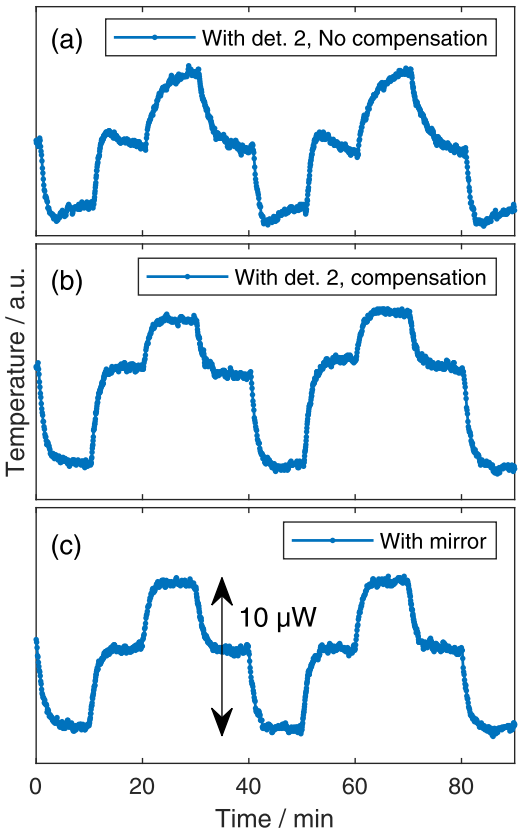

Figure 10. (a) Temperature signal of the target detector showing drift effects caused by heating of the monitor detector during optical heating. (b) Temperature signal when applying a small electrical power to the monitor detector during electrical heating, to maintain a constant temperature flow from the monitor detector.
(c) Temperature signal when replacing the monitor detector with a mirror. The arrow indicates the power difference between the high and low electrical step.

for maintaining a constant temperature level throughout the electrical substitution mode.

The total power of step (b) (optical + electrical) is found from equation (3), in the same way as for the OC method. The optical power is then determined by subtracting $P_{\mathrm{el}} = VI$ from the total power, where V is the measured voltage across and I is the measured current running through the photodiode during illumination.

The applied voltage for each step was chosen such that the step size was the same as in OC mode (5 μW), with the optical power level placed between the two electrical power levels. The additional electrical heating during optical heating was 100 μW.

6. Calculation algorithms

Despite using a temperature controller on the copper trap structure, it is not possible to achieve an absolutely stable temperature. For this reason we want to use a calculation algorithm that will give reliable results independent of background drift. We have here included a study of three different drift compensating algorithms. The local average method involves averaging

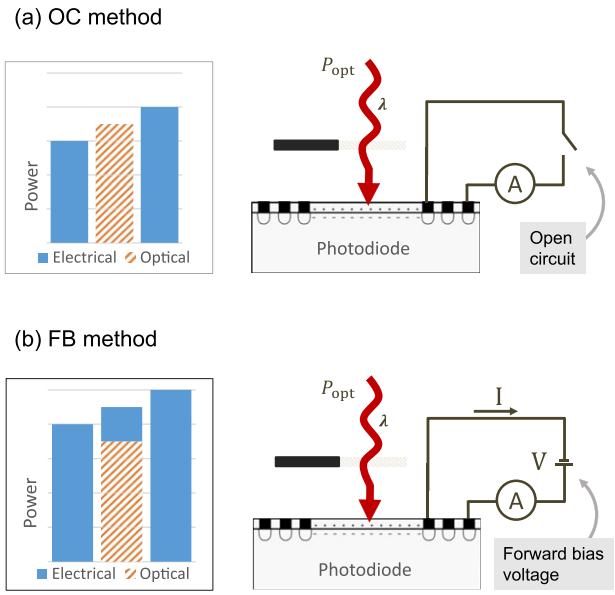

Figure 11. Schematic showing heating steps for (a) the OC method with OC during optical heating, and (b) the FB method with additional electrical heating from forward biasing the photodiode during optical heating.

the heating steps locally around one electrical high or low heating level. The drift correction method involves a piece-wise linear correction to the temperature signal, while the exponential fit method fits the temperature change between the heating levels to an exponential function and determines the saturation temperature from the fit function.

6.1. Local average method

The local average calculation algorithm is illustrated in figure 12. The figure shows the temperature signal for two cycles of electrical substitution, going through low electrical, optical and high electrical heating. The temperature value from each step was found by averaging the last 120 s of the interval. In figure 12(a), T_1, P_1 and T_{opt} are found by averaging two successive low electrical heating steps and two optical heating steps. T_2 and P_2 are determined from the high electrical level between the two optical levels. These values are then put into equation (3) to determine the optical power for this cycle, $P^j_{\mathrm{opt,A}}$. A similar averaging is done with two high electrical levels and two optical levels, as shown in figure 12(b), giving $P^j_{\mathrm{opt,B}}$.

Since all measurement points are equally spaced in time and the averaging is symmetrical around the middle level, the calculated values for each level are projected to the same point in time. This ensures compensation for drift, when assuming linear drift over the time span of one cycle. One measurement point, P^j_{opt}, corresponds to an average of $P^j_{\mathrm{opt,A}}$ and $P^j_{\mathrm{opt,B}}$, and the optical power from thermal mode is found from an average of n measurement points:

$$P^j_{\mathrm{opt}} = \frac{1}{2}(P^j_{\mathrm{opt,A}} + P^j_{\mathrm{opt,B}}), \tag{9}$$

$$P_{\mathrm{opt}} = \frac{1}{n}\sum_j P^j_{\mathrm{opt}}. \tag{10}$$

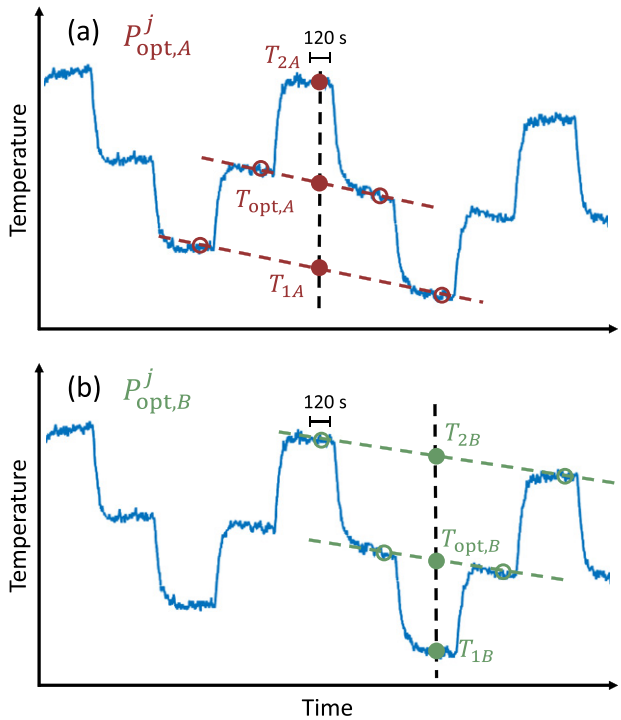

Figure 12. Illustration showing the local average calculation algorithm for finding the optical power from thermal mode, P_{opt}, from equation (3). (a) $P^j_{\mathrm{opt,A}}$ is found by averaging two successive low electrical heating steps and two optical heating steps. (b) $P^j_{\mathrm{opt,B}}$ is found by averaging two successive high electrical heating steps and two optical heating steps. One measurement point corresponds to an average of $P^j_{\mathrm{opt,A}}$ and $P^j_{\mathrm{opt,B}}$.

The uncertainty of P^j_{opt}, $u(P^j_{\mathrm{opt}})$, is propagated through the calculations from the standard deviation for each of the last 120 s of the measured signal level.

6.2. Drift correction method

The second method we studied uses a linear fit to correct the temperature data. One way to do this is to evaluate the entire dataset in one piece. However, in our case, for every low electrical heating level, the applied power is well-known and given by $P = VI$. Hence, any difference between the temperature of two low or high electrical levels must be caused by drift in the background temperature. This means that the electrical heating levels can serve as anchor points in the linear fit, and independent fits can be done between each anchor point. Fragmenting the linear correction in this way means that we have to assume linear drift only between each anchor point (as in the local average method described above), not for the entire dataset. We defined the anchor point of the jth cycle as the average of the measurement points from the last 120 s of the low electrical heating. Between two anchor points, the correction ΔT from the linear fit is given by:

$$\Delta T = T_0 - [m_j(t - t_{0,j}) + T_j], \tag{11}$$

where T_0 is the mean of the 120 last seconds in the first cycle, t is the elapsed time, m_j is the slope of the linear fit, $t_{0,j}$ is the time of the first data point in the correction of the jth cycle,

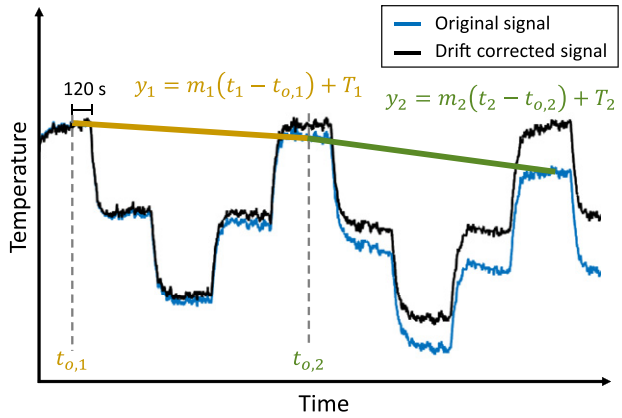

Figure 13. Illustration showing the drift correction method, using a piece-wise linear fit to correct the background drift in temperature.

and T_j is the temperature value at time $t_{0,j}$. This is illustrated in figure 13. Corrected temperature values are given by:

$$T'_i = T_i + \Delta T. \tag{12}$$

When the data is drift corrected, an average of each temperature level can be calculated in the following way:

$$T_x = \frac{1}{n \cdot N} \sum_i^{n \cdot N} T'_i, \tag{13}$$

where T_x denotes the temperature at each of the three levels T_1, T_{opt} and T_2, n is the number of thermal cycles and N is the number of measurement points in the last 120 s of the level. The average power of the electrical levels are given by

$$P_x = \frac{1}{n \cdot N} \sum_i^{n \cdot N} P_i, \tag{14}$$

where P_x is P_1 and P_2, P_i is the product of the voltage V_i and the current I_i in each data point. The values calculated from equations (13) and (14) are then inserted into equation (3) to determine the absorbed optical power P_{opt} from thermal mode. The uncertainty was calculated the same way as for the local average method, by the propagated standard deviation of the measured signals over the last 120 s, including the uncertainty contribution from the linear fit.

6.3. Exponential fit method

We also performed an exponential fit to the drift corrected data presented in section 6.2. By doing this, we could estimate the saturation level of the temperature signal from the fit directly, which then became a third calculation algorithm. The data was fitted to the following exponential function, using MATLAB [25]:

$$M(\boldsymbol{c}, t) = c_1 \, \mathrm{e}^{-z_1 t} + c_2, \quad \boldsymbol{c} = \begin{pmatrix} z_1 \\ c_1 \\ c_2 \end{pmatrix}, \tag{15}$$

where t is time and z_1, c_1 and c_2 are fitting parameters. A fit was performed for each heating step, and the input values for equation (3), T_1, T_2 and T_{opt}, were determined by c_2. By

this method all data points are used in the extraction of the saturation level c_2. The associated time constant is $\tau = 1/z_1$.

The uncertainty was estimated by propagating the observed standard deviation of each measurement point as compared to the fit function. This is done with matrix evaluation as explained in [26] when the value of interest is a subfunction of the fit function based on the method given by [27]. Using the variance of each of the measurement points to the fit function enables estimation of the uncertainty in the measurement points without having to do multiple measurements at each point and ensures simultaneously to include a possible lack of fit to the propagated uncertainty.

7. Results and discussion

7.1. Thermal time constant—simulation and experiment

The thermal time constant of the heat link was calculated from the exponential fit to the temperature signal, as described in section 6.3, on drift corrected temperature signals described in section 6.2. Results for the mean time constant of each thermal step are shown in figure 14. The time constant for the different steps are equal within the error bars, which represents the propagated standard deviation ($k = 1$). The values shown are averages for 12 different measurement series, with an average of 20 heating cycles per measurement series. The average value of the time constant is 65.3 s ± 8.0 s. This is around 20 s lower than that predicted by simulations, and this difference between simulated and measured time constant was surprisingly high. This may be due to differences between dimensions of the fabricated assembly and the simulated model as well as between used and actual material properties. However, it may also indicate that some effects are overlooked and not fully understood.

7.2. Non-equivalence vs vertical alignment—simulation and experiment

Figure 15 shows the apparent IQD and simulated non-equivalence as a function of beam spot position on the photodiode. The results for three different calculation algorithms are shown, and a discussion on these can be found in the following section. The measurements were performed with optical power of 1250 μW, using the FB method (see section 5.4) with an additional 100 μW electrical heating. The simulations predict that the IQD should vary as a function of the optical beam's vertical position by about 280 ppm per millimeter. As the figure shows, the experimental results follow the same slope as the simulated non-equivalence. The grey points show the IQD when corrected for the non-equivalence.

For $y = 0$ and $y = 0.5$ mm, measurements were done before and after removing a dust particle from the window surface of the vacuum cube using a puffer. After removing the dust particle, the measured IQD was reduced by about 130 ppm in both positions. This can be explained by scattered light from the dust particle hitting outside the active area of the photodiode. This light will produce a thermal signal, but not a photocurrent, which gives an increase in the apparent IQD.

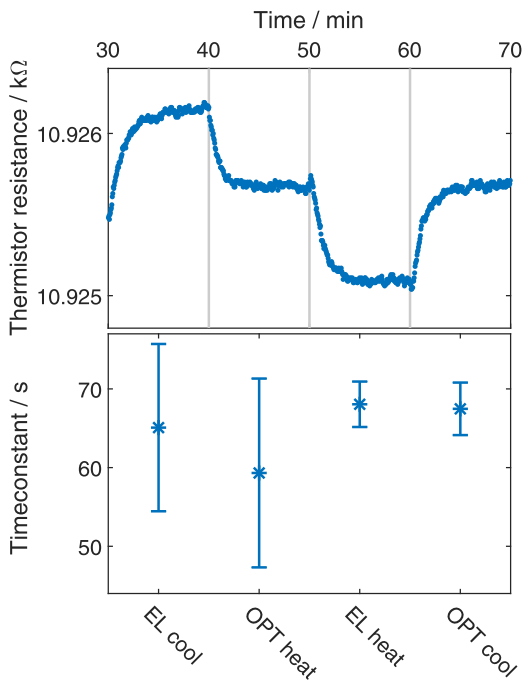

Figure 14. Top: example of temperature signal for calculating time constants. Bottom: calculated time constants for the four sections shown above, averaged over all measured cycles.

The double measurement at position $y = -1.5$ mm is the result of a change in polarity in the electrical current measurement in the experiment. Photocurrent in the second measurement goes in the opposite direction as the photocurrent measurement in the first measurement and same as the electrical heating in the first measurement. The deviation between the two measurements is below 10 ppm, confirming that no significant offsets in the electrical measurements are present. Furthermore, the agreement at this level re-confirms the estimated uncertainty in the measurements.

However, the measured IQD values are around 400 ppm higher than the expected IQD of the photodiode, which is in the order of 10 ppm or better [19], indicating that there are some additional error sources present. This may partly be attributed to an uncertainty in our method for locating the middle point of the photodiode without any alignment marks, partly a difference due to offsets from deviations in real and simulated heating profiles and partly some residual window scatter and other unknown offsets.

7.3. Comparing measurement algorithms

Figure 15 shows results from the dual-mode measurement using the three different algorithms: the local average method, drift correction and exponential fit method. Error bars show the propagated type A standard uncertainty.

As seen from the figure, all three methods agree within the uncertainty in all measurement points. The exponential fit method shows a trend of estimating a lower IQD in most of the points. This could be caused by inclusion of more data points, as the exponential fit method exploits data points from all 10 min of each thermal step rather than just the last 2 min.

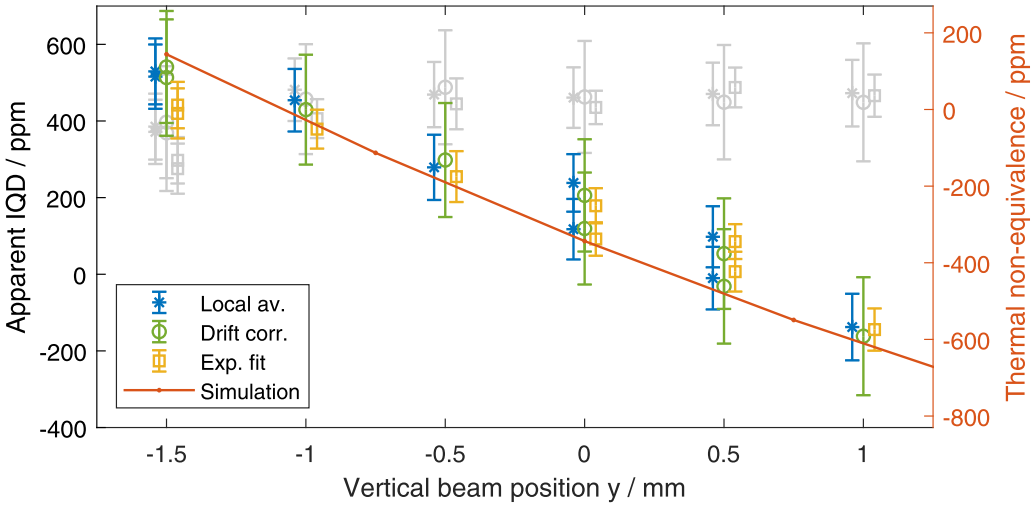

Figure 15. Apparent IQD (left axis) as a function of beam position on the photodiode with error bars showing propagated type A standard uncertainty. Solid line shows the thermal non-equivalence predicted from simulation (right axis). Measurements were performed using the FB method with optical power of 1250 μW and additional electrical power of 100 μW. Grey points show the IQD when corrected for the thermal non-equivalence.

This also explains the lower uncertainty for the exponential fit method, as inclusion of data from the entire thermal step gives more rigidity to the model and benefit from an averaging effect. An effort was also made to include an additional exponential term in the fit function (15). However, this produced results with large variation and not in agreement with the other methods. Interestingly, this method indicates that two time constants of around 20 s and 65 s are present, which is not supported by thermal simulations. This may be related to the deviation between the experimental and simulated time constant and possible knock-on effects on thermal equivalence.

The agreement between the three calculation algorithms shows that they can all be used to get a reliable result. The exponential fit method has the advantage of lower uncertainty, and might be preferential when a clean temperature curve is available. The downside is that it is more time consuming and slightly more complex to implement than the other two methods.

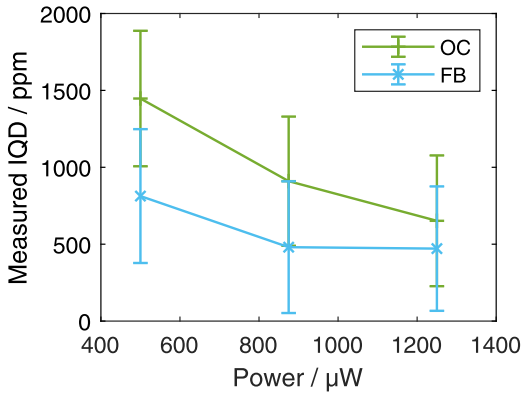

Figure 16. Measured IQD as a function of absorbed optical power for the two different methods of electrical substitution—OC during optical heating (OC method, green pluses) and FB/electrical heating during optical heating (FB method, blue crosses), using the exponential fit algorithm. The additional electrical heating for the FB method was 100 μW, and error bars show the combined standard uncertainty ($k = 1$).

7.4. Measured IQD—Comparison of OC and FB method

The measured IQD for the two different operational modes during electrical substitution, OC and FB, are shown in figure 16 as a function of absorbed optical power. The calculation algorithm used here is the exponential fit method, described in section 6.3, and the error bars show the combined uncertainty. The laser beam was aligned onto the centre of the photodiode, corresponding to $y = 0$ in figure 5(a). It is worth noticing that the measurements presented in figure 16 were done before removal of the dust particle, which introduced an offset of about 130 ppm, as discussed in the previous section. According to the simulations of non-equivalence, the positioning of the beam spot (in centre) will lead to an offset of about 343 ppm. The results in figure 16 have been corrected for the non-equivalence offset as well as the 130 ppm offset from the dust particle. However, the latter might be power dependent, which could explain the increase in IQD for lower power levels seen in the graph.

The type A standard uncertainty for the exponential fit algorithm is similar for both methods and below 50 ppm in all points, and around 30 ppm for the FB method at 1250 μW. There seems to be an increasing discrepancy between the OC and FB methods for lower power levels. It is unlikely that this effect is related to the dust particle, as it will affect how much light is seen by the detector, which will be the same for both methods. The consistently higher measured IQD for the OC method compared to the FB method indicates that there is additional heating in the optical thermal measurement despite an OC. One possible explanation is that generated charge carriers, though steady state in time, will not recombine in the same location as they are generated. The spatial charge transportation inside the photodiode may generate a small additional heat.

Table 1. Uncertainty budget for optical power measured with thermal mode, P_{opt}, for 488 nm wavelength at 1250 μW power level, with the beam spot in $y = -1$ mm from the photodiode centre. The optical power is calculated from a mean of five measurement cycles, each with a calculated value P^j_{opt}, and the table presents type A values from the first measurement cycle. The type B uncertainty contributions listed are thermal non-equivalence d_{noneq}, alignment of the beam unto the photodiode d_{align}, stray light d_{stray}, heating of the mirror d_{mirror}, and instrument offsets d_{instr}.

	X_i	x_i	$u(x_i)$	c_i	$u_i(y)$
Type A	T_{opt}	10 847.514 Ω	0.0027 Ω	−0.0090 mW Ω^{-1}	2.4×10^{-5} mW
	T_1	10 848.033 Ω	0.0036 Ω	0.0048 mW Ω^{-1}	1.7×10^{-5} mW
	T_2	10 846.910 Ω	0.0049 Ω	0.0042 mW Ω^{-1}	2.0×10^{-5} mW
	P_1	1.352 93 mW	1.5×10^{-6} mW	0.537 86	7.8×10^{-7} mW
	P_2	1.363 01 mW	2.9×10^{-6} mW	0.462 14	1.3×10^{-6} mW
	$P^{\mathrm{FB}}_{\mathrm{opt}}$	0.107 40 mW	1.3×10^{-6} mW	1	1.3×10^{-6} mW
	$P^i_{\mathrm{opt}} =$	1.250 19 mW			3.6×10^{-5} mW
	$P^n_{\mathrm{opt}} = \frac{1}{n}\sum_j P^j_{\mathrm{opt}}$	1.250 44 mW	$u(P^j_{\mathrm{opt}})$	$1/\sqrt{n} = 1/\sqrt{5}$	1.6×10^{-5} mW
Type B	d_{noneq}	2.7×10^{-6}	1×10^{-4}	P^n_{opt}	1.2×10^{-4} mW
	d_{align}	0	1.4×10^{-4}	P^n_{opt}	1.6×10^{-4} mW
	d_{stray}	5×10^{-5}	5×10^{-5}	P^n_{opt}	6.3×10^{-5} mW
	d_{mirror}	0	7×10^{-6}	P^n_{opt}	8.8×10^{-5} mW
	d_{instr}	0.0012 mW	5×10^{-5} mW	1	2.5×10^{-5} mW
	P_{opt}	1.2518 mW		$k = 1$	2.3×10^{-4} mW
				$k = 2$	4.6×10^{-4} mW

Table 2. Uncertainty budget for the self-calibration measurement for 488 nm wavelength at 1250 μW, where thermal mode is used as a reference to determine the IQD $\delta(\lambda)$. The uncertainty contribution $d_{\mathrm{instr,ph}}$ represents offsets and uncertainties in the measurement instruments.

	X_i	x_i	$u(x_i)$	c_i	$u_i(y)$
Type A	P_{opt}	1.2518 mW	2.3×10^{-4} mW	0.7985 mW^{-1}	1.8×10^{-4}
	i_{photo}	0.4920 mA	1.5×10^{-5} mA	−2.030 mA^{-1}	3.1×10^{-5}
	λ	487.98 nm	1×10^{-2} nm	2×10^{-3} nm^{-1}	2.2×10^{-7}
Type B	$d_{\mathrm{instr,ph}}$	4.5×10^{-4} mA	2×10^{-5} mA	−2.030 mA^{-1}	4.1×10^{-5}
	d_{yield}	-1.7×10^{-5} mA	3×10^{-5} mA	−2.030 mA^{-1}	6.0×10^{-5}
	$\delta(\lambda)$	5.35×10^{-4}		$k = 1$	1.97×10^{-4}
				$k = 2$	3.94×10^{-4}

In the FB method, an electrical power is applied at all times throughout the thermal mode. Hence, the results in figure 16 demonstrate the feasibility to maintain a constant temperature by adjusting the electrical power in a closed feedback loop.

7.5. Uncertainty evaluation

Table 1 shows the uncertainty budget of the thermal mode of the dual-mode measurement, for 1250 μW absorbed power at 488 nm wavelength, with the beam spot in $y = -1$ mm from the photodiode centre. The measurand in table 1, the optical power from thermal mode, is given by:

$$P_{\mathrm{opt}} = P^n_{\mathrm{opt}}(1 + d_{\mathrm{noneq}} + d_{\mathrm{mirror}} + d_{\mathrm{stray}}) + d_{\mathrm{instr}}. \tag{16}$$

Here each d corresponds to an uncertainty contribution.

The thermal signals are shown in the table as the thermistor resistance reading from the measurement bridge with typical standard deviation. The type A uncertainty from five cycles of thermal measurements at 1250 μW absorbed power is 16 nW, a relative type A uncertainty of 13 ppm. The electrical power is calculated from the product of the measured current and voltage. The uncertainty d_{noneq} of 100 ppm accounts for the spread in simulated non-equivalence due to uncertainty in material properties as well as variations in beam profile and geometrical dimensions, such as thicknesses of the various components. The thermal simulations predict a non-equivalence of 27 ppm with the beam spot in position $y = -1$ mm. As the thermal non-equivalence depends on the position of the beam, knowledge of the position is necessary to keep the influence of thermal non-equivalence to a minimum. The dependence on non-equivalence by beam position is reflected in d_{align}, with an assumed error of 0.5 mm in the beam position corresponding to a 0.35 mm uncertainty in vertical position. With a change in non-equivalence of 280 ppm mm^{-1}, this gives an uncertainty contribution of 140 ppm.

Stray light d_{stray} is added as an offset, as light absorbed outside the active area of the photodiode will contribute to the thermal measurement and not to the photocurrent measurement. It is worth noting that replacement of the monitor detector with a mirror, as discussed in section 5.3, introduces slightly more stray light into the vacuum cube. Thermal influence from the mirror was calculated based on the thermal influence from the monitor detector. With the ratio of reflectance between mirror and photodiode as a scaling factor, an estimate of 7 ppm was reached for d_{mirror}. The last type B term, d_{instr}, is determined from calibration of the measurement instruments involved.

From table 1 it can be seen that the main contributor to the uncertainty is the alignment, d_{align}. The alignment procedure was not optimised during this experiment, and we believe this number can be reduced with about an order of magnitude by using a more thorough alignment procedure. The second largest contributor, d_{noneq}, can be reduced by validating the thermal non-equivalence against an external reference. Stray light d_{stray}, which also include window effects, can be reduced by replacing the wedged window with a Brewster window.

Table 2 shows the uncertainty budget for the estimated IQD, with the measurand given by:

$$\delta(\lambda) = 1 - \frac{(i_{\text{photo}} + d_{\text{instr, ph}} + d_{\text{yield}})}{P_{\text{opt}}} \frac{hc}{e\lambda}, \tag{17}$$

where $d_{\text{instr,ph}}$ is the uncertainty in the instruments for measuring the photocurrent, d_{yield} is the quantum yield correction estimated from data in [22] and P_{opt} is determined by equation (16).

The photocurrent is typically 0.4920 mA at 1250 μW with a standard deviation of $\sim 5 \times 10^{-5}$ mA. The estimated IQD from the dual-mode self-calibration measurement at 1250 μW is 535 ppm with an expanded standard uncertainty of 394 ppm.

8. Conclusion

We have developed a self-calibrating room temperature dual-mode detector for absolute radiometric measurements. In this work we have presented results from the self-calibration procedure, giving an estimate for the internal losses of the photodiode at different power levels. The study consists of design and simulations of heat equivalence of packaged dual-mode photodiodes, realisation of dual-mode modules, their implementation and assembly in a trap structure and experimental characterisations of the dual-mode modules. Two different operational methods were tested, and the results from both methods agree within the uncertainty. The work demonstrated from the FB method that it is feasible to apply the dual-mode method in closed feedback loop operation. Also, three different calculation algorithms were compared. The agreement in values and uncertainties between all three algorithms confirms the calculations.

The non-equivalence sensitivity to beam position of 280 ppm mm^{-1} predicted from thermal simulations were experimentally confirmed. The predicted time constant was ~20 s shorter than the simulated time constant of 86 s. The reason for this may be deviations in the physical realisation of the packaged dual-mode detector, but may also indicate that there are unknown contributors to the non-equivalence.

The work revealed that the fractional heat from absorbed optical power in the monitor photodiode in a trap structure influenced the thermal reading on the target photodiode and had to be handled despite the mounting in a massive copper trap structure. The work further revealed that a localised single dust particle on the vacuum cube window influenced the IQD measurement by more than 100 ppm. Offsets from the electronic current direction was not observed as the measurements with reversed current configuration reproduced the measured IQD to within 10 ppm.

The IQD of the photodiode was extracted using the FB dual-mode self-calibration method, and at 1250 μW the IQD was found to be 535 ppm ± 394 ppm ($k = 2$). This is high compared to the expected IQD of 20 ppm or less. This suggests that there are unknown offsets or effects not yet understood. A dominating uncertainty contribution is the thermal non-equivalence, which in this study was estimated using computer simulations. The true non-equivalence will be validated in future work by comparison to an external reference, such as a CR. This will also provide a validation of the true IQD.

A type A standard uncertainty of around 13 ppm was observed for absorbed power of 1250 μW at 488 nm for five thermal cycles using the exponential fit method. This is remarkably low at room temperature and is ensured from a considerable effort in noise reduction in the setup. The low type A uncertainty ensures production of steady results, which is the key for revealing possible unknown errors or offsets in the future.

The aim of the present study was to establish a measurement realisation of the dual-mode self-calibration procedure to an uncertainty of 500 ppm. Our work has shown that we are well within this target for the power levels studied and that we can produce measurements at the same level as the CR at room temperature when careful alignment of the dual mode detector is optimised.

Acknowledgments

This project 18SIB10 chipS·CALe has received funding from the EMPIR programme co-financed by the Participating States and from the European Union's Horizon 2020 research and innovation programme.

ORCID iDs

Marit S Ulset https://orcid.org/0000-0002-8320-7511
Eivind Bardalen https://orcid.org/0000-0001-7469-8585
Roberto Filippo https://orcid.org/0000-0003-3184-3687
Mauro Rajteri https://orcid.org/0000-0001-6712-5658
Meelis-Mait Sildoja https://orcid.org/0000-0001-7787-4214
Toomas Kübarsepp https://orcid.org/0000-0002-7304-427X

References

[1] Fox N P and Martin J E 1990 Comparison of two cryogenic radiometers by determining the absolute spectral responsivity of silicon photodiodes with an uncertainty of 0.02% *Appl. Opt.* **29** 4686–93

[2] Geist J 1979 Quantum efficiency of the p–n junction in silicon as an absolute radiometric standard *Appl. Opt.* **18** 760–2

[3] Zalewski E F and Geist J 1980 Silicon photodiode absolute spectral response self-calibration *Appl. Opt.* **19** 1214–6

[4] Hansen T E 1978 Silicon UV-photodiodes using natural inversion layers *Phys. Scr.* **18** 471–5

[5] Geist J, Zalewski E F and Schaefer A R 1980 Spectral response self-calibration and interpolation of silicon photodiodes *Appl. Opt.* **19** 3795–9

[6] Geist J, Brida G and Rastello M L 2003 Prospects for improving the accuracy of silicon photodiode self-calibration with custom cryogenic photodiodes *Metrologia* **40** S132–5

[7] Geist J, Robinson A M and James C R 1991 Numerical modeling of silicon photodiodes for high-accuracy applications, part III: interpolating and extrapolating internal quantum-efficiency calibrations *J. Res. Natl. Inst. Stand.* **96** 481–92

[8] Gentile T R, Houston J M and Cromer C L 1996 Realization of a scale of absolute spectral response using the National Institute of Standards and Technology high-accuracy cryogenic radiometer *Appl. Opt.* **35** 4392–403

[9] Gentile T R, Brown S W, Lykke K R, Shaw P S and Woodward J T 2010 Internal quantum efficiency modeling of silicon photodiodes *Appl. Opt.* **49** 1859–64

[10] Gran J 2005 Accurate and independent spectral response scale based on silicon trap detectors and spectrally invariant detectors *PhD Thesis* University of Oslo

[11] Rastello M L *et al* 2011 The Qu-Candela project http://www.quantumcandela.org/

[12] Sildoja M *et al* 2013 Predictable quantum efficient detector: I. Photodiodes and predicted responsivity *Metrologia* **50** 385–94

[13] Müller I *et al* 2013 Predictable quantum efficient detector: II. Characterization and confirmed responsivity *Metrologia* **50** 395–401

[14] Gran J, Kübarsepp T, Sildoja M, Manoocheri F, Ikonen E and Müller I 2012 Simulations of a predictable quantum efficient detector with PC1D *Metrologia* **49** S130–4

[15] BIPM 2015 Mise en pratique for the definition of the candela and associated derived units http://bipm.org/en/publications/mises-en-pratique

[16] White M, Gran J, Tomlin N and Lehman J 2014 A detector combining quantum and thermal primary radiometric standards in the same artefact *Metrologia* **51** S245–51

[17] Nordsveen M U, Tang C K and Gran J 2017 Demonstration of a dual-mode Si detector as a self-calibrating device at room temperature *Opt. Express* **25** 8459–69

[18] Gran J *et al* 2022 The chipS CALe project http://chipscale.aalto.fi

[19] Koybasi O *et al* 2021 High performance predictable quantum efficient detector based on induced-junction photodiodes passivated with SiO_2/SiN_x *Sensors* **21** 7807

[20] Tran T *et al* 2022 Determination of the responsivity of predictable quantum efficient detector over a wide spectral range based on a 3D model of charge carrier recombination losses *Metrologia* https://doi.org/10.1088/1681-7575/ac604b

[21] Brida G, Geist J and Rastello M L 2002 A proposal for the experimental check of the Josephson equality Kj = 2e/h private communication.

[22] Werner L *et al* 2021 Quantum yield in induced junction silicon photodiodes at wavelengths around 400 nm *14th Int. Conf. on New Developments and Applications in Optical Radiometry (NEWRAD 2021)*

[23] Monte C and Hollandt J 2010 The measurement of directional spectral emissivity in the temperature range from 80 °C to 500 °C at the Physikalisch-Technische Bundesanstalt *High Temp.–High Press.* **39** 151–64

[24] Monte C and Hollandt J 2010 The determination of the uncertainties of spectral emissivity measurements in air at the PTB *Metrologia* **47** 172

[25] Nielsen H B 2010 Immoptibox - A MATLAB toolbox for optimization and data fitting http://www2.imm.dtu.dk/projects/immoptibox/Manual.pdf

[26] Gran J and Sudbø A S 2004 Absolute calibration of silicon photodiodes by purely relative measurements *Metrologia* **41** 204–12

[27] Lira I 2000 Curve adjustment by the least-squares method *Metrologia* **37** 677–81